Editors' Suggestion

Nanoindentation simulations for copper and tungsten with adaptive-precision potentials

David Immel
Jülich Supercomputing Centre (JSC), Forschungszentrum Jülich, Jülich, Germany

Matous Mrovec and Ralf Drautz
Interdisciplinary Centre for Advanced Materials Simulations (ICAMS), Ruhr Universität Bochum, Bochum, Germany

Godehard Sutmann*
Jülich Supercomputing Centre (JSC), Forschungszentrum Jülich, Jülich, Germany
and Interdisciplinary Centre for Advanced Materials Simulations (ICAMS), Ruhr Universität Bochum, Bochum, Germany

(Received 19 May 2025; accepted 30 July 2025; published 26 September 2025)

We perform nanoindentation simulations for both the prototypical face-centered cubic metal copper and the body-centered cubic metal tungsten with an adaptive-precision description of interaction potentials including different accuracy and computational costs. We combine both a computationally efficient embedded atom method (EAM) potential and a precise but computationally less efficient machine learning potential based on the atomic cluster expansion (ACE) into an adaptive precision (AP) potential tailored for the nanoindentation. The numerically more expensive ACE potential is employed selectively only in regions of the computational cell where high precision is required. The comparison with pure EAM and pure ACE simulations shows that for Cu, all potentials yield similar dislocation morphologies under the indenter with only small quantitative differences. In contrast, markedly different plasticity mechanisms are observed for W in simulations performed with the central-force EAM potential compared to results obtained using the ACE potential. ACE is able to describe accurately the angular character of bonding, which is in W due to its half-filled *d* band. All ACE-specific mechanisms are reproduced in the AP nanoindentation simulations, however, with a significant speedup of 20–30 times compared to the pure ACE simulations. Hence, the AP potential overcomes the performance gap between the precise ACE and the fast EAM potential by combining the advantages of both potentials.

DOI: 10.1103/2lkd-l6gt

I. INTRODUCTION

Large-scale molecular dynamics (MD) simulations of nanoindentations [1,2] can provide valuable insights into microscopic mechanical behavior of metallic materials and reveal underlying mechanisms that govern initial stages of plastic deformation. To obtain trustworthy results, it is essential to describe the atomic interactions with accurate and transferable interatomic potentials [2]. For free-electron metals with close-packed face-centered cubic (fcc) crystal structures, many-body central force approaches, such as the embedded atom method (EAM) [3] or the Finnis-Sinclair potentials [4], usually describe the metallic bonding sufficiently accurate. However, many transition metals with partially filled *d* bands cannot be described properly by such central-force models [5–12]. These metals, crystallizing in hexagonal close-packed (hcp) or body-centered cubic (bcc) structures, require explicit descriptions of their directional (and thus angular-dependent) bonding.

Two prototypical elements representing these families of metals are fcc copper (Cu) and bcc tungsten (W). Understanding mechanical properties of both metals at the nanoscale is highly relevant due to ever-increasing miniaturization. The refractory metal W is also considered as a plasma facing material (PFM) for next generation fusion reactors [13–15]. As PFMs need to sustain extreme operating conditions, understanding changes of their mechanical properties due to formation of a large number of crystal defects under irradiation is of utmost importance. Even though nanoindentation simulations have already provided valuable mechanistic insights into microscale plasticity for both Cu [16–19] and W [20–25], further investigations and validations with improved interatomic potentials are still needed, especially for bcc W.

In recent years, machine-learning (ML) potentials proved to be able to deliver an accuracy close to that of first-principles electronic-structure methods at a fraction of their computational cost [26–30]. Even though there exist ML potentials for Cu [27] and W [31–35], their application to large-scale nanoindentation simulations is still limited. One contributing reason is that most ML potentials remain several orders of magnitude slower than the simple empirical potentials [27,36,37].

A possible solution how to maintain desired accuracy while improving computational efficiency is by coupling different interaction models. Typically, a more accurate but computa-

*Contact author: g.sutmann@fz-juelich.de

tionally demanding model is used for a small portion of the simulated system where decisive processes take place (for instance, bond breaking at a crack tip, surface reactions, or defect nucleation sites). An efficient but less accurate model is then applied for remaining parts of the simulated system where only small variations are expected (for instance, maintaining a long range elastic field or temperature gradients). A well-known and widely applied example is coupling of quantum-mechanical (QM) approaches with molecular mechanics (MM), which originated almost 50 years ago [38]. Current QM/MM implementations are able to adjust both regions during simulations based on various criteria [39–41]. When QM calculations are not required, the coupling can also be done for interatomic potentials with different levels of accuracy and computational cost [42–45].

A viable way to overcome the performance gap between ML and simple empirical potentials is via the adaptive precision (AP) method [42]. In the AP method, the potential energy is a weighted average of the combined potentials depending on a switching parameter. The switching parameter is calculated by a customizable detection mechanism so the assignment of atoms to a particular region can be done in an automatized way. Thus, the method works autonomously and self-adaptively in space and time. An important feature of the AP method is that the time integration of the equations of motion maintains the conservation of energy and momentum.

In this work, we apply the AP method to combine the speed of EAM potentials and the accuracy of atomic cluster expansion (ACE) potentials in large-scale nanoindentation simulations. Furthermore, we extend the original approach to account properly for homogeneous nucleation of dislocations that takes place below the indenter in regions of highest shear stress [46]. These events marking the onset of plasticity need to be simulated with the accurate ACE potential.

II. METHODS

A. Nanoindentation

The MD simulations were performed using the LAMMPS software package [47]. One of common approaches in the nanoindentation simulations is to separate the simulation block into three parts [21,22,48], as visualized in Fig. 1. The bottom part is kept fixed to prevent rotation and translation of the sample, the central part is simulated using the *NVT* ensemble to dissipate heat generated by the indentation, and the top part is simulated using the *NVE* ensemble. The spherical rigid indenter was described by the following potential [49]:

$$V_{\text{ind}}(\vec{r}) = \frac{k_{\text{ind}}}{3}\Theta(R_{\text{ind}} - |\vec{r}_{\text{ind}} - \vec{r}|)(R_{\text{ind}} - |\vec{r}_{\text{ind}} - \vec{r}|)^3, \quad (1)$$

where k_{ind} is the force constant, $\vec{r}_{\text{ind}}(t)$ the center of the indenter, R_{ind} the indenter radius, and $\Theta(x)$ the Heaviside step function. In the beginning of the simulation, the indenter and surface are not in contact and the center of the indenter is located at $\vec{r}_{\text{ind},0}$. The indenter is then gradually inserted into the sample with a constant velocity $\vec{v}_{\text{ind}}$ such that its position changes as $\vec{r}_{\text{ind}}(t) = \vec{r}_{\text{ind},0} - \vec{v}_{\text{ind}}t$. Further details about simulation setup are provided in Appendix A.

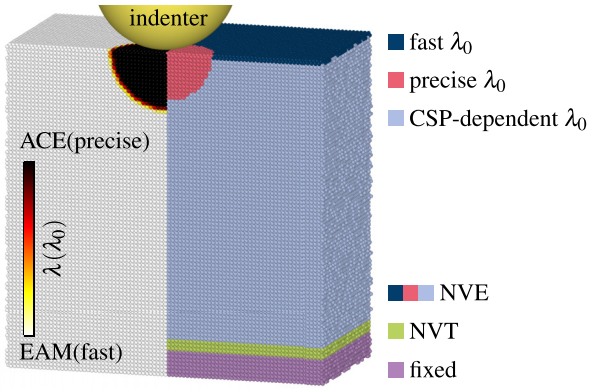

FIG. 1. Cut through the system along the (100) plane below the indenter. Right side: The top atoms (■■■) are simulated in a *NVE* ensemble, the bottom atoms are fixed (■), and the atoms in between are simulated in a *NVT* ensemble (■). For simulations with an adaptive-precision potential, the parameter λ_0 is used to calculate the switching parameter λ, which is required to calculate the potential energy according to Eq. (5). To ensure a precise simulation, $\lambda_0 = 0$ is set after the equilibration for all atoms which are in a hemisphere (■) whose center is on the surface of the material under the center of the indenter. The centrosymmetry parameter (CSP) is used to calculate λ_0 for most atoms (■) to dynamically adjust the precision. To save the computation time, $\lambda_0 = 1$ is set at the surface outside of the hemisphere (■) to prevent the detection of the surface by the CSP. Left side: Initially used switching parameter λ calculated from λ_0. A region of interest below the indenter is calculated precisely while the remaining atoms are calculated quickly

B. Interatomic potentials

1. Embedded atom method

In the EAM potentials used in this work, the energy of an atom i is given as

$$E_i^{\text{EAM}} = \xi\left(\sum_{j\neq i}\zeta(r_{ij})\right) + \frac{1}{2}\sum_{j\neq i}\Phi(r_{ij}), \quad (2)$$

where ξ is the embedding function, ζ is the electron charge density, and Φ is the pair potential. For Cu, we used the EAM2 parametrization of Ref. [50], which has been thoroughly tested and widely used [51–54]. For W, we used the EAM2 potential from Ref. [55], which was developed for simulating radiation defects and dislocations and is widely used [21,56–58].

2. Atomic cluster expansion

The employed ACE potentials used a combination of linear and square-root expansions that were shown to give the best accuracy and computational performance [27]. The potential energy of an atom i described by ACE is given as

$$E_i^{\text{ACE}} = \phi_i^{(1)} + \sqrt{\phi_i^{(2)}}. \quad (3)$$

The functions $\phi_i^{(p)}$ are expanded as

$$\phi_i^{(p)} = \sum_{\boldsymbol{v}} c_{\boldsymbol{v}}^{(p)} B_{i\boldsymbol{v}}, \quad (4)$$

where B_{iv} are product basis functions, which describe the atomic environment, and $c_{\boldsymbol{v}}^{(p)}$ are fitted expansion coefficients with the multi-indices $\boldsymbol{v}$. For Cu, we used the ACE parametrization developed in Ref. [27], which is widely used [59–61], for example, in dislocation simulations [62]. For W, we used an ACE parametrization trained on an extensive DFT dataset of bulk structures as well as defects. Further information of this potential is provided in Appendix B 2.

3. Adaptive-precision potential

The atomic energy of the AP potential [42], which combines EAM and ACE, is given by

$$E_i = \lambda_i E_i^{\mathrm{EAM}} + (1-\lambda_i) E_i^{\mathrm{ACE}}, \tag{5}$$

where $\lambda_i \in [0, 1]$ is the switching parameter [42]. We used the switching parameter based on the centrosymmetry parameter (CSP) [49] to detect atoms which need to be treated with the more accurate potential. In addition, we fixed the value of λ_i in specific regions of the simulation block, as visualized in Fig. 1. Since the first dislocations nucleate primarily in the regions of highest shear stress near the indenter surface [46], the region below the indenter is always simulated with the ACE potential. In practice, we set the initial value of $\lambda_{0,i} = 0$ in a hemisphere of radius 40 Å whose center is at the contact point where the indenter first touches the surface. Additionally, to prevent the CSP from detecting surface atoms, we set $\lambda_{0,i} = 1$ for surface atoms which are outside of the ACE hemisphere. For the remaining atoms, $\lambda_{0,i}$ is calculated based on the CSP and $\lambda_i(\{\lambda_{0,j}\})$ is calculated as described in Ref. [42]. Using this setup, we minimize the amount of the computationally more expensive ACE calculations. During later stages of the simulation, λ_i is recalculated and updated [42]. For Cu, we use parametrization Hyb1, which we developed in our previous paper [42]. The AP potential for W is described in Appendix B.

III. RESULTS

A. Copper

Before staring the nanoindentation simulation, we equilibrate the $\mathrm{Cu}_{(100)}$ surface as described in Appendix A. The nanoindentation simulation is then performed using the NVE ensemble, but a thin layer of atoms at the bottom of the simulation box is thermostated and the very bottom layers are kept fixed to dissipate heat generated during the indentation and to prevent translation and rotation of the sample, as visualized in Fig. 1. The fundamental parameters of the simulation are summarized in Table I.

The nanoindentation simulations were carried out on the JURECA-DC supercomputer [63]. The speedup of the AP nanoindentation simulation compared to that performed with ACE only is about 21, as shown in Fig. 2. The fixing of the switching parameter in the zones of interest, as described in Sec. II B 3, results in a speedup of 1.9 of the AP simulation compared to the AP simulation in Ref. [42]. Further details of the computational efficiency are provided in Appendix C.

The displacement of the surface atoms which developed during the nanoindentations with the three potentials is visualized in Figs. 3(a)–3(c). The height of the surface on a line through the contact point of surface and indenter is shown for cross sections along the ⟨110⟩ and ⟨100⟩ directions in Fig. 3(d). We observe small pileups in the ⟨110⟩ directions, similarly to Ref. [18], and no pileup in the ⟨100⟩ directions.

TABLE I. Parameter values used in the copper nanoindentation simulations.

Parameter	Value
Surface orientation	(100)
Temperature	292 K
Simulation box size	364.2 Å × 364.2 Å × 363.2 Å
Number of atoms	4 000 000
Height of fixed region	10 Å
Height of NVT region	10 Å
Timestep Δt	1 fs
Indenter radius R_{ind}	60 Å
Indenter velocity $\vec{v}_{\mathrm{ind}}$	$\{0, 0, 25\}$ m/s
Indenter force constant k_{ind}	10 eV Å^{-3}
Indentation depth h_{max}	20 Å
Initial indentation depth h_0	−5 Å

The force between an atom i and the indenter is given as $\vec{F}_{\mathrm{ind}}(\vec{r}_i) = -\vec{\nabla}_{|\vec{r}_{\mathrm{ind}}-\vec{r}|} V_{\mathrm{ind}}(\vec{r}_i)$, with V_{ind} according to Eq. (1). The indentation load

$$P_{\mathrm{ind}} = \sum_i \vec{F}_{\mathrm{ind}}(\vec{r}_i) \cdot \frac{\vec{v}_{\mathrm{ind}}}{v_{\mathrm{ind}}} \tag{6}$$

is given as total force on all atoms in the indentation direction $[00\bar{1}]$ and automatically calculated during the simulation. The Hertzian analysis [64–66] is applied to evaluate the Hertzian load P_{H} on the surface as a function of the indentation depth h as

$$P_{\mathrm{H}} = \tfrac{4}{3} E^* R_{\mathrm{ind}}^{1/2} h^{3/2}, \tag{7}$$

where R_{ind} is the indenter radius and E^* the indentation modulus. This formula does not consider elastic anisotropy of materials, but it holds for spherical indenters with a modified indentation modulus [66–68]. The Hertz fit allows us to detect the onset of plastic deformation. Both the simulated load P_{ind} and the fitted analytical solution P_{H} are shown in Fig. 4(a). The fits give $E^*_{\mathrm{EAM}} = 115.9$ GPa, $E^*_{\mathrm{AP}} = 116.1$ Gpa and $E^*_{\mathrm{ACE}} = 112.0$ GPa and are thus similar for all potentials.

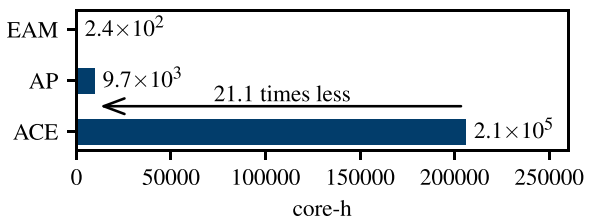

FIG. 2. Total computation time of a nanoindentation with 4×10^6 Cu atoms simulated for 100 ps with the AP potential compared to ACE and EAM simulations. EAM, AP, and ACE simulations are calculated on 128, 128, and 2048 cores of JURECA-DC [63], respectively.

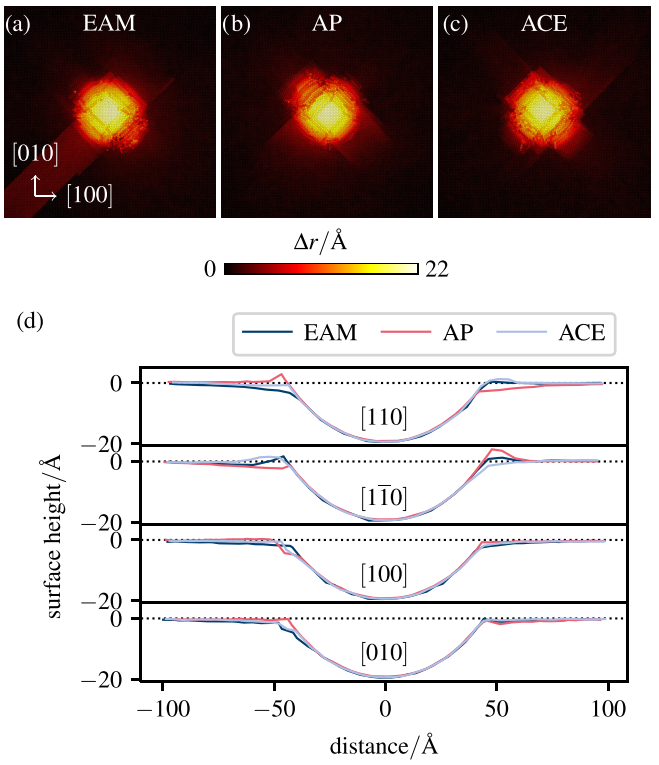

FIG. 3. (a)–(c) Displacement Δr of the copper atoms at 20 Å indentation depth compared with −5 Å indentation depth. (d) Cross sections through the center of the supercell below the indenter along different directions at 20 Å indentation depth.

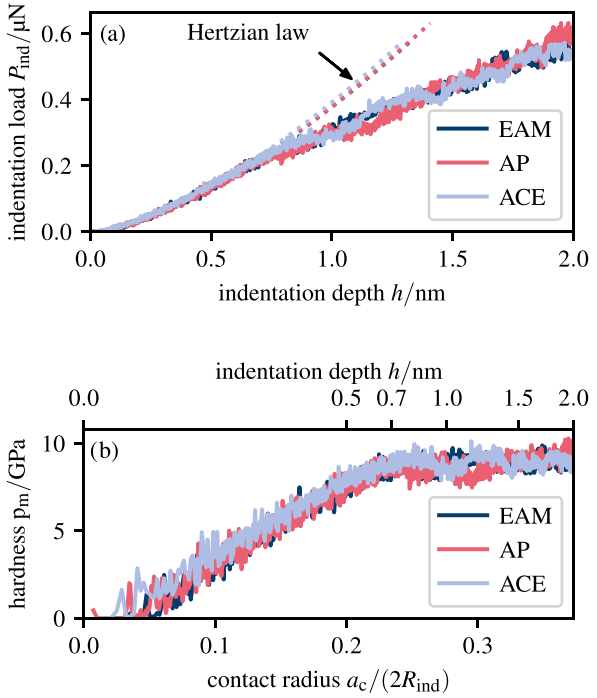

FIG. 4. (a) Indentation load P_{ind} and elastic Hertzian load P_H according to Eqs. (6) and (7) computed for the copper nanoindentations. (b) Mean contact pressure or hardness p_m according to Eq. (8) dependent on the contact radius a_c according to Eq. (9). The contact radius is normalized with the radius R_{ind} of the spherical indenter.

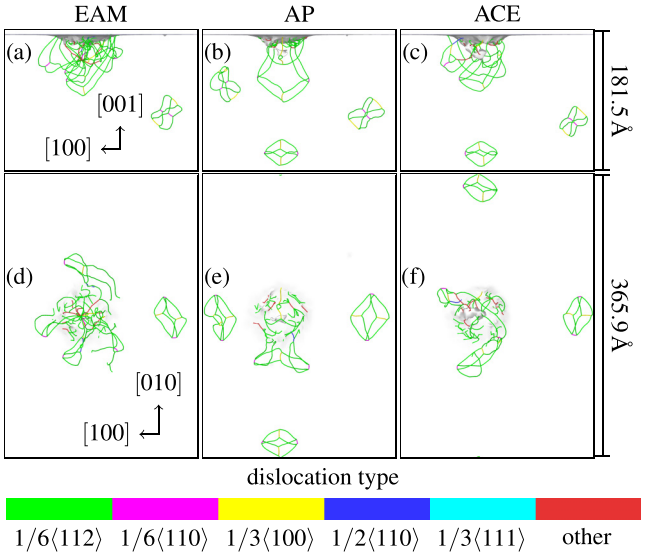

FIG. 5. Dislocation lines in Cu identified by the DXA analysis of OVITO for a normalized indentation depth of $h/a_c \approx 0.34$. The dislocation lines are color-coded according to their identified dislocation type. A scale bar is given on the right side for every row.

The hardness or mean contact pressure p_m on the surface is

$$p_m = \frac{P_{ind}}{A_c} = \frac{P_{ind}}{\pi a_c^2}, \tag{8}$$

where A_c is the projected contact area with the contact radius a_c. There are different models for the contact radius [17,18,69]. We use the contact radius

$$a_c = \sqrt{h(2R_{ind} - h)}, \tag{9}$$

as this model was applied in nanoindentation simulations of Cu [18] and W [22] with spherical rigid indenters and thus enables a seamless comparison of our results with the literature. The mean contact pressure p_m is shown in Fig. 4(b). It increases linearly until plastic deformation sets in at $a_c/(2R_{ind}) \approx 0.23$ and reaches a steady state for larger contact radii. This behavior is independent of the interatomic potential used, as expected from Refs. [21,69]. The average hardness at the steady state is 8.9 GPa with a standard deviation up to 0.5 GPa. The hardness reported for $Cu_{(100)}$ in Ref. [18] is 11.7 ± 1.4 GPa and thus somewhat higher, but the indenter velocity was two times faster than in our case; as the hardness increases with the indenter velocity [70,71], a larger hardness magnitude is therefore expected.

The dislocation extraction algorithm (DXA) [72] implemented in OVITO [73] was used to calculate the dislocation length l_{klm} of dislocations of type klm. For the fcc lattice, DXA identifies dislocations with the Burgers vectors $1/6\langle 112\rangle$, $1/6\langle 110\rangle$, $1/3\langle 100\rangle$, $1/2\langle 110\rangle$, $1/3\langle 111\rangle$, and other Burgers vectors. Dislocation networks observed in the simulations for the indentation depth $h/a_c \approx 0.34$ are shown in Fig. 5.

Prismatic dislocation loops nucleate as in Ref. [18] for all potentials. The prismatic dislocation loops glide in the directions $[10\bar{1}]$, $[\bar{1}0\bar{1}]$, $[01\bar{1}]$, and $[0\bar{1}\bar{1}]$. Five dislocation loops

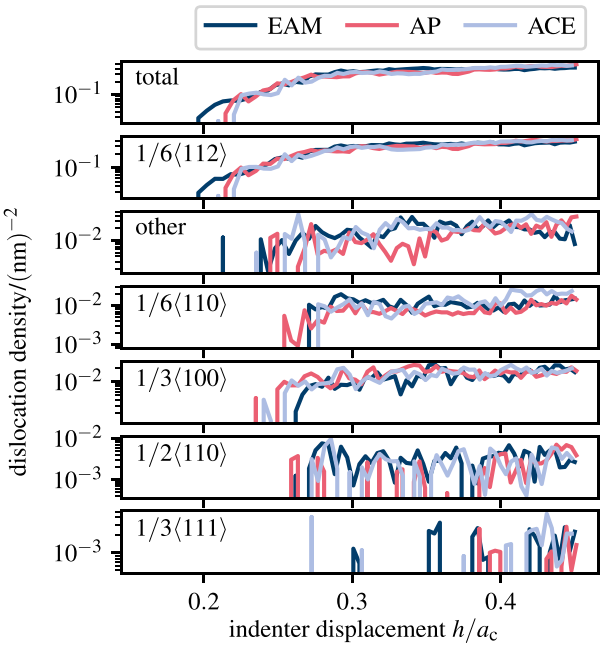

FIG. 6. Dislocation density according to Eq. (10) for nanoindentations of $Cu_{(100)}$. The dislocation density is given for all by the DXA of OVITO identified dislocation types. Furthermore, the total type-independent dislocation density is shown.

nucleate during the simulation for EAM while four nucleate for the AP potential and ACE.

The dislocation density

$$\rho_{klm}^{\mathrm{dxa}} = l_{klm}/V^{\mathrm{dxa}} \tag{10}$$

is calculated within the effective volume V^{dxa} of the plastic zone. The radius a_{pz} of the plastic zone is given by

$$a_{\mathrm{pz}} = f_{\mathrm{pz}} a_{\mathrm{c}}, \tag{11}$$

where the factor $f_{\mathrm{pz}} \in [0, 3.5]$ depends on the material [74]. For Cu, we used $f_{\mathrm{pz}} = 1.9$ [75]. Thus, the effective volume of the plastic zone is given by $V^{\mathrm{dxa}} = 2\pi a_{\mathrm{pz}}^3/3 - V_{\mathrm{ind}}$, where the volume V_{ind} displaced by the indenter, without considering sink-in and pileup effects, is given as $V_{\mathrm{ind}} = \pi h^2(R_{\mathrm{ind}} - h)/3$ [21,76]. The densities of different dislocation types as a function of the indentation depth are shown in Fig. 6. As expected, the first nucleated dislocation has the Burgers vector $1/6\langle 112\rangle$ for all potentials, but the nucleation occurs earlier for EAM than for the AP potential and ACE. We observe all dislocation types being nucleated for all potentials.

The shear strain was evaluated using OVITO according to the method described in Ref. [77], where the initial configuration was used as a reference. The shear strain is visualized at the end of the simulations in Fig. 7. The red slip traces in Figs. 7(a)–7(c) in the $[10\bar{1}]$ and $[\bar{1}0\bar{1}]$ directions with a shear strain of about 0.3 mark the glide of prismatic dislocation loops. Furthermore, a wedge-shaped dislocation develops close the surface in the EAM simulation [see Fig. 7(d)] as in Ref. [19] and glides in the $[\bar{1}\bar{1}0]$ direction. This leads to $1/2[\bar{1}\bar{1}0]$ atomic displacements which are visible at the surface in Fig. 3(a).

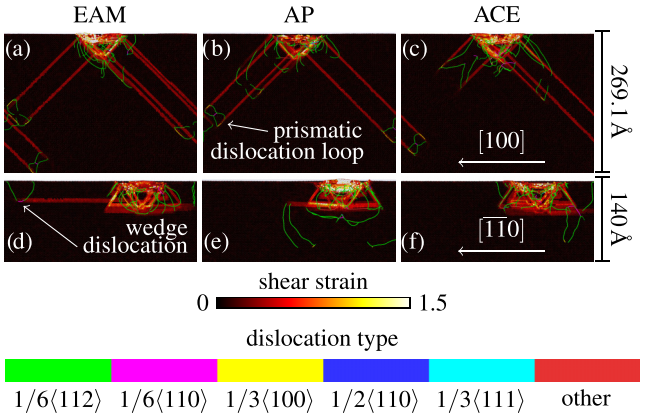

FIG. 7. The copper atoms are color-coded according to the shear strain evaluated using OVITO in the (a)–(c) (010) and (d)–(f) $(1\bar{1}0)$ plane through the contact point for a normalized indentation depth of $h/a_{\mathrm{c}} \approx 0.45$. The dislocation lines computed with the DXA analysis of OVITO are shown for 35 Å in the normal direction of the corresponding plane and color-coded according to their dislocation type. A scale bar is given on the right side for every row.

B. Tungsten

The nanoindentation simulation for W was carried out in equivalent manner as that for Cu. The parameters of the simulation are given in Table II. The speedup of the AP simulation compared to the ACE simulation is 27.1, as shown in Fig. 8. Details regarding the computational efficiency are provided in Appendix C.

The displacement of the surface atoms between initial and maximum indentation depth is visualized in Figs. 9(a)–9(c). In contrast to Cu, the observed surface pattern from the EAM simulation differs markedly from those of the AP and ACE simulations. For EAM, marked pileups are observed along the ⟨110⟩ directions while for AP and ACE the surfaces around the indenter remain almost flat. The variations of the surface height are plotted for different cross sections through the contact point of surface and indenter in Fig. 9(d). EAM shows a pileup of about 10.2 ± 1.3 Å in the ⟨110⟩ directions while small depressions develop in the AP and ACE simulations.

TABLE II. Parameters and the used values in the tungsten nanoindentations performed with molecular dynamics simulations.

Parameter	Value
Surface orientation	(100)
Temperature	300 K
Initial box size	273.1 Å × 273.1 Å × 271.9 Å
Number of atoms	1 272 112
Height fixed region	20 Å
Height *NVT* region	10 Å
Time step Δt	1 fs
Indenter radius R_{ind}	60 Å [21]
Indenter velocity $\vec{v}_{\mathrm{ind}}$	{0, 0, 20}m/s [21]
Indenter force constant k_{ind}	236 eVÅ^{-3} [21]
Indentation depth h_{max}	20.8 Å
Initial indentation depth h_0	−4.2 Å

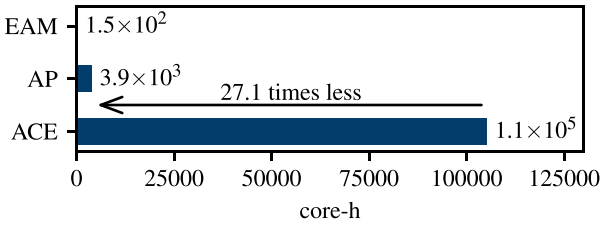

FIG. 8. Total computation time of a nanoindentation with 1 272 112 W atoms simulated for 125 ps using the AP potential compared to ACE and EAM simulations. EAM, AP and ACE simulations are calculated on 128, 128, and 640 cores of JURECA-DC [63], respectively.

Our results can be compared with those of other nanoindentation simulations [21,78] that used the same rigid spherical indenter and the same indentation velocity. In these studies, several interatomic potentials, including a tabulated Gaussian approximation potential (tabGAP) [33] were systematically compared. The tabGAP potential is an ML potential [79] which contains up to three-body descriptors and was extensively tested for various defects in W [33]. Similar to our study, pileups were found for the EAM potential while surface depressions were predicted by tabGAP at 30 Å indentation depth [78].

The Hertzian loads P_{H} fitted to the indentation loads P_{ind} according to Eq. (7) are plotted in Fig. 10(a). The obtained indentation moduli of 519.0 GPa for EAM, 458.2 GPa for AP, and 452.9 GPa for ACE confirm the consistency of AP and ACE simulations.

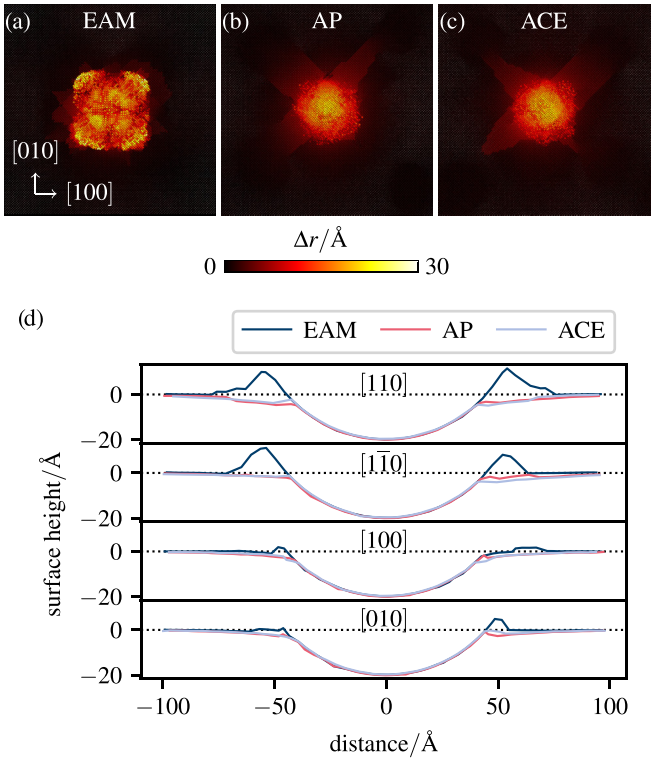

FIG. 9. (a)–(c) Displacement Δr of the W atoms at 20.8 Å indentation depth compared with −4.2 Å indentation depth. (d) Cross sections through the center of the supercell below the indenter along different directions at 20.8 Å indentation depth.

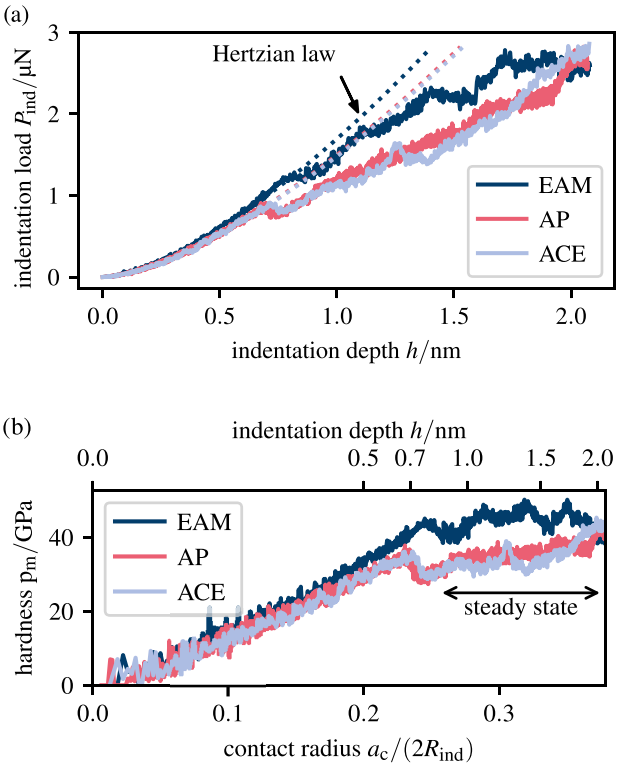

FIG. 10. (a) Indentation load P_{ind} and elastic Hertzian load P_{H} according to Eqs. (6) and (7) computed for the W nanoindentations. (b) Mean contact pressure or hardness p_{m} according to Eq. (8) dependent on the contact radius a_{c} according to Eq. (9). The contact radius is normalized by the radius R_{ind} of the spherical indenter.

The hardness calculated according to Eq. (8) is shown in Fig. 10(b). The sample deforms elastically until $h \approx 8.3$ Å, 7.0 Å, and 7.4 Å for EAM, AP, and ACE simulations, respectively. The hardness values in the steady state of plastic deformation are 44.3 ± 2.6 GPa for EAM, 35.6 ± 3.0 GPa for the AP potential, and 35.1 ± 4.1 GPa for ACE. The pileup, which develops in the EAM simulation, increases the contact radius while the surface depression in the AP and ACE simulations reduces the contact radius. Neither of these effects is incorporated in the analytical model of the contact radius in Eq. (9). Thus, the hardness is overestimated in the EAM simulation compared to the AP and ACE simulations, which is consistent with the observed values. Our hardness values are comparable with the value of 37.8 GPa reported in Ref. [22] for another EAM potential [80], where the indentation velocity of 50 m/s and the force constant of 10 eVÅ^{-3} were applied.

A convenient tool to identify defects in bcc materials is the bcc defect analysis (BDA) [81], which has been employed for inspection of several nanoindentation simulations [21,82]. The BDA identification is based on common neighbor analysis [83], coordination number, and centrosymmetry parameter. The algorithm can identify surface atoms, atoms next to a vacancy, screw and nonscrew dislocations, {110} planar faults, and twin boundaries. The screw dislocations and twin boundaries cannot be distinguished by BDA, but the line character of

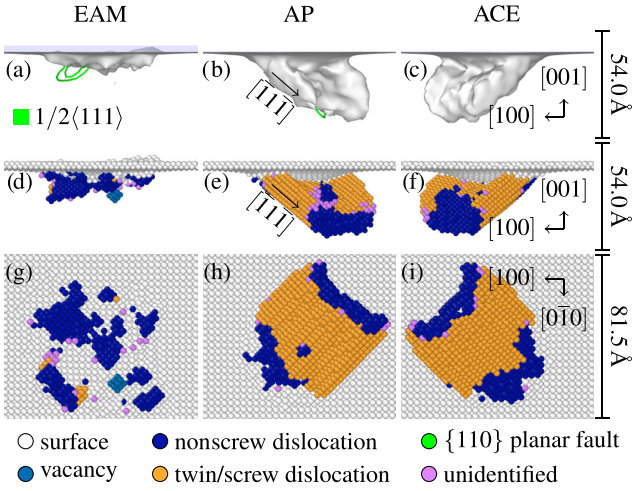

FIG. 11. Visualization of dislocation lines using the DXA algorithm of OVITO (a)–(c) and bcc defects identified by BDA (d)–(i) for a normalized indentation depth of $h/a_c \approx 0.41$. In BDA, the atoms are color-coded according to the identified defect type while perfect bulk atoms are not shown. A scale bar is given on the right side for every row.

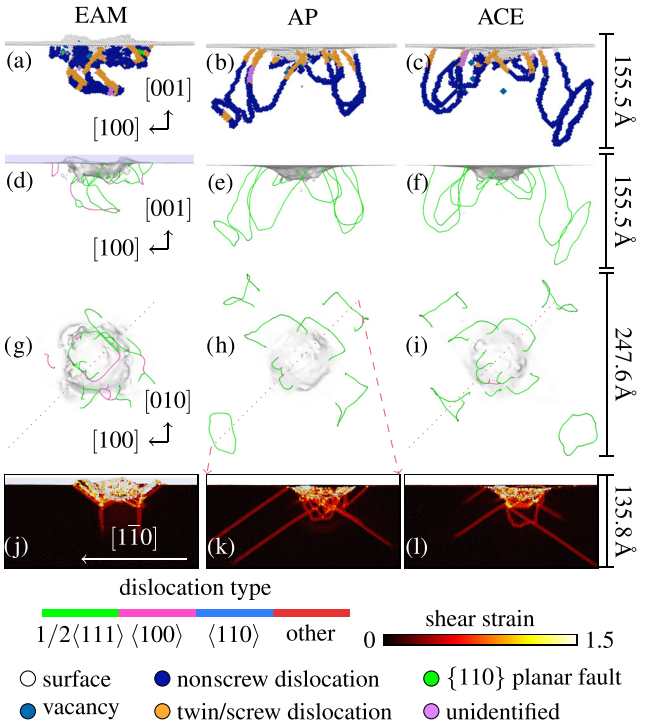

FIG. 12. (a)–(c) Visualization of the atoms detected by the bcc defect analysis for the maximum normalized indentation depth of $h/a_c \approx 0.62$. (d)–(i) Visualization of the dislocation lines identified by the dislocation extraction algorithm viewed from different perspectives. The dotted line visualizes the (110) plane. (j)–(l) A cut in this plane through the system is used to visualize the by OVITO calculated shear strain. Scale bars are given on the right side of each row. The visualizations in the first column are from the EAM simulation, the second column contains the ones of the adaptive-precision (AP) simulation and the ACE simulation is shown in the third column.

screw dislocations and planar character of twin boundaries can be discerned easily by a visual inspection. Since deformation twinning may compete with dislocation-mediated plasticity in W nanocrystals [84], BDA provides a complementary view to the detection of dislocation lines with DXA. Both DXA and BDA visualizations for the normalized indentation depth $h/a_c \approx 0.41$ are shown in Fig. 11. Furthermore, the DXA and BDA results for the maximum indentation depth $h/a_c \approx 0.62$ are shown in Fig. 12.

For EAM, two $1/2\langle 111\rangle$ dislocation loops are visible in Fig. 11(a), as they emerge from the highly distorted region below the indenter. In contrast, a deformation twin develops initially in both AP and ACE simulations. The twin structures grow in the $\langle 111\rangle$ directions on the {211} habit planes. Eventually, the twin propagation stops and $1/2\langle 111\rangle$ dislocation loops start to nucleate from the twin tip, as visible in Fig. 11(b). This process likely occurs by coalescence of three $1/6\langle 111\rangle$ twinning dislocations and leads to gradual retraction of the twin and transformation of the twinned region into a dislocation network. At the maximum indentation depth, as shown in Figs. 12(b) and 12(c), only dislocation loops are present below the indenter. Such incipient nanocontact plasticity via nucleation, propagation, and annihilation of twins has been reported in simulations of bcc Ta [85]. A similar outcome was also observed in the recent tabGAP simulations [21], but some twins were still present at the maximum indentation depth of 30 Å while all twins transformed into dislocation lines in our simulations. The initial twinning deformation was not observed for any other classical potentials used in Ref. [21].

Dislocation lines identified by the DXA and BDA approaches are shown in Fig. 12 for the maximum indentation depth of $h/a_c \approx 0.62$. While DXA can distinguish bcc dislocations with the $1/2\langle 111\rangle$, $\langle 100\rangle$ and $\langle 110\rangle$ Burgers vectors, BDA can resolve only the $1/2\langle 111\rangle$ screw and nonscrew types. The dislocation network in EAM simulations differs markedly from those in AP and ACE simulations. In the latter simulations, one can almost exclusively see dislocations with the shortest $1/2\langle 111\rangle$ Burgers vector. The dislocation half loops emanating from the indented region consist of long segments of predominantly screw character connected by a curved mixed/edge segment. The presence of long screws is expected due to their large Peierls stress and thermally activated motion. The half loops propagate away from the indenter and their interaction leads in some cases to formation of prismatic dislocation loops, as observed also in Ref. [21]. These loops continue to glide in the $\langle 111\rangle$ directions as evidenced by the slip lines in Figs. 12(k) and 12(l).

In contrast, there are no extended dislocation segments or $\langle 111\rangle$ loops observed in the EAM simulation, as shown in Fig. 12(d). Instead, the dislocation network is concentrated primarily right under the indenter with significant portion of $\langle 100\rangle$ dislocations that glide in the $[00\bar{1}]$ direction normal to the surface, as visible on the slip traces in Fig. 12(j). This observation is consistent with results from Ref. [21], where $\langle 100\rangle$ shear loops, which nucleated below the indenter and glided in the $[00\bar{1}]$ direction, were observed in simulations that used the same EAM potential and indenter but a larger indentation depth.

The dislocation density is calculated according to Eq. (10). For this, we need the radius a_{pz} of the plastic zone

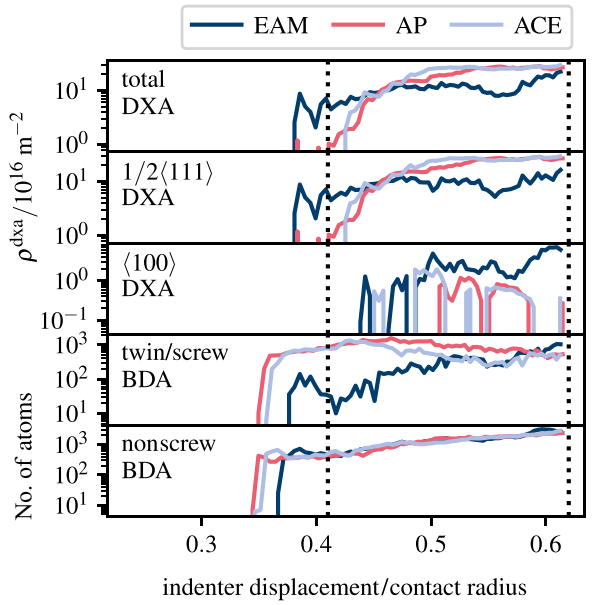

FIG. 13. Dislocation density evaluated using DXA and BDA analyses for nanoindentations of $W_{(100)}$. Since BDA cannot distinguish twins and screw dislocations, only their sum is given. The dashed vertical lines mark the indentation depths analyzed in Figs. 11 and 12.

according to Eq. (11), where the material-dependent factor $f_{\mathrm{pz}} = 1.9$ is used for W [21]. The dislocation density as a function of the indentation depth is shown in Fig. 13. Furthermore, the plot also includes defect analysis using the BDA algorithm. The number of twins/screw dislocations has a maximum at 0.47 and 0.43 for the AP and ACE simulations, respectively. This is consistent with the visual analysis discussed above, since twins gradually transform to $1/2\langle 111\rangle$ dislocations. Thus, Fig. 13 confirms the transition from initial twin-mediated plasticity to dislocation-mediated plasticity in the AP and ACE simulations. For EAM, there is only dislocation-mediated plasticity. Furthermore, one can clearly see the different mechanisms of dislocation-mediated plasticity between EAM simulation and ACE/AP simulations. The density of $\langle 100\rangle$ dislocations remains high during the course of the EAM simulation while these dislocations are only intermittent in the ACE/AP simulations.

IV. CONCLUSION

In this work, we systematically compared results of nanoindentation simulations for the prototypical fcc metal copper and bcc metal tungsten performed with interatomic potentials of different accuracies and computational costs. We employed computationally efficient EAM potentials, accurate but less efficient machine learning ACE potentials, and an AP combination of both [42]. The selection of atoms treated by the AP potential was extended and compared to our previous work to ensure an accurate description of atoms whose environment differs significantly from that of bulk crystal.

Our results show that for Cu, all potentials yield similar dislocation morphologies under the indenter with only small quantitative differences. This confirms that the EAM potential can describe well the metallic bonding in free-electron metal Cu. Therefore, despite the achieved speedup of 21.1 of the AP simulation compared to the ACE simulation, one does not gain additional insights from the additional accuracy offered by the ACE potential in this case.

In contrast, markedly different plasticity mechanisms were observed for W in simulations performed with the central-force EAM potential compared to results obtained using the ACE potential, which is able to accurately describe the angular character of the directional bonding, which is caused by the half-filled d band of W. The EAM potential (also with optimized parameters as shown in Appendix D) predicts dislocation-mediated plasticity and sustained presence of the $\langle 100\rangle$ dislocations below the indenter. In the ACE simulations, we instead observed a transition from initial twin-mediated plasticity to dislocation-mediated plasticity and predominance of the common $1/2\langle 111\rangle$ dislocations. All ACE-specific mechanisms were reproduced in the AP nanoindentation simulations, however, with a significant speedup of almost 30 times compared to the ACE-only simulations. Hence, the AP potential overcomes the performance gap between the precise ACE and the fast EAM potential by combining the advantages of both potentials. Thus, AP potentials are beneficial for materials where simple central-force models are not appropriate, such as for the description of the directional bonds in bcc transition metals.

ACKNOWLEDGMENTS

We thank A. Bochkarev for providing the preliminary ACE parametrization for tungsten. The authors gratefully acknowledge computing time on the supercomputer JURECA [63] at Forschungszentrum Jülich under Grant No. 28990 (hybridace).

The authors declare no competing interests.

D.I. provided formal analysis (equal), investigation (equal), methodology (equal), resources (equal), software (lead), validation (equal), visualization (lead), and writing of the original draft (lead). M.M. provided formal analysis (equal), investigation (equal), methodology (equal), validation (equal), writing of the original draft (supporting), and writing–review and editing (lead). R.D. provided conceptualization (equal), methodology (equal), supervision (equal), and writing—review and editing (supporting). G.S. provided conceptualization (equal), methodology (equal), resources (equal), supervision (equal), and writing—review and editing (supporting).

DATA AVAILABILITY

Our adaptive-precision interatomic potentials (APIP) package is available as part of LAMMPS and contains our modifications to the LAMMPS source code, which allows the usage of the APIP. LAMMPS is available in Ref. [87]. The staggered-grid domain decomposition for LAMMPS will be published separately in the future, but the APIP package does not depend on the geometry of the spatial domain decomposition [86] and can also be used with the load balancing via recursive coordinate bisectioning [91], which is implemented in LAMMPS [47].

APPENDIX A: EQUILIBRATION

We use a relaxation technique adapted from Refs. [48,88]. First, a perfect lattice is created at 0 K. The perfect lattice is simulated with periodic boundary conditions in all dimensions as a *NVT* ensemble with a Langevin thermostat with the damping constant γ^{L} until the temperature is within the tolerance δ_T to the target temperature T_{targ}. In the second step, a *NPT* ensemble is simulated according to Nosé-Hoover with damping parameters γ_T^{NH} and γ_p^{NH} for temperature and pressure until target temperature and target pressure p_{targ} are within the tolerance δ_T and δ_p of the target values. At this target temperature and pressure, the surface is created at the top of the simulation box in the z direction and the open boundary conditions are used instead. The bottom atoms in the z direction are frozen at their current positions and their velocity is set to zero and not updated anymore. In a third simulation of the duration Δt_{E}, a *NVT* ensemble with a Langevin thermostat is applied. The thermostat damps the pressure waves of the created surface. The total momentum is set to zero repeatedly after the time interval Δt_{mom} since it is not conserved by the Langevin thermostat. All equilibration steps and the nanoindentation itself are simulated with the time step Δt.

Dynamic load balancing is essential for the adaptive-precision simulations as the time required to calculate forces and energies for a particle heavily depends on the used interatomic potential. We use a staggered grid [89] as spatial domain decomposition [86], which is balanced by ALL [90] as described in Ref. [42]. For the EAM and ACE simulation, we use the recursive coordinate bisectioning (RCB) [91] from LAMMPS which balances the LAMMPS tiled domain layout according to the measured force-calculation time. The load balancer is called after every time interval Δt_{RCB} or Δt_{SG} if the system is imbalanced enough.

All mentioned parameters are listed in Table III for the copper and tungsten simulations with all three interatomic potentials.

TABLE III. Parameters used during the three steps of equilibration and during the nanoindentation as described in Appendix A.

	Copper			Tungsten		
Property	EAM	AP	ACE	EAM	AP	ACE
Step 1: *NVT* periodic boundaries						
γ^{L}/ps	1	1	1	1	1	1
δ_T/K	0.2	0.2	0.2	0.2	0.2	0.2
Step 2: *NPT* periodic boundaries						
δ_p/bar	10	10	10	10	10	10
γ_T^{NH}/ps	0.1	0.1	0.1	0.1	0.1	0.1
γ_p^{NH}/ps	1	1	1	1	1	1
p_{targ}/bar	0	0	0	0	0	0
Step 3: *NVT* surface						
Δt_{E}/ps	50	50	50	100	2	100
γ^{L}/ps	10	10	10	0.1	0.1	0.1
Δt_{mom}/ps	1	1	1	1	1	1
Step 4: Nanoindentation						
γ_T^{NH}/ps	0.1	0.1	0.1	0.1	0.1	0.1
All steps						
T_{targ}/K	292	292	292	300	300	300
Δt/ps	0.001	0.001	0.001	0.001	0.001	0.001
Δt_{RCB}/ps	0.1		0.1	0.1		0.1
Δt_{SG}/ps		0.025			0.025	

APPENDIX B: AP POTENTIAL FOR TUNGSTEN

1. EAM potential

We used the EAM potential for W developed in Ref. [55], which is given by the embedding function

$$\xi(x) = a_1^{\xi}\sqrt{x} + a_2^{\xi}x^2, \tag{B1}$$

the pair potential

$$\Phi(x) = \sum_{i=1}^{n^{\Phi}} a_i^{\Phi}\left(\delta_i^{\Phi} - x\right)^3 \Theta\left(\delta_i^{\Phi} - x\right), \tag{B2}$$

and the electron charge density

$$\zeta_0(x) = \sum_{i=1}^{n^{\zeta}} a_i^{\zeta}\left(\delta_i^{\zeta} - x\right)^3 \Theta\left(\delta_i^{\zeta} - x\right), \tag{B3}$$

where $\Theta(x) = 1$ for $x \geqslant 0$, 0 for $x < 0$. The electron charge density $\zeta_0(r)$ becomes negative for small r and has a maximum at r_{cut}^{ζ}. Thus, a constant value of the electron charge density is used in the form of

$$\zeta(x) = \begin{cases} \zeta_0(r_{\mathrm{cut}}^{\zeta}) & \text{for } r \leqslant r_{\mathrm{cut}}^{\zeta} \\ \zeta_0(r) & \text{for } r > r_{\mathrm{cut}}^{\zeta} \end{cases} \tag{B4}$$

to ensure a continuous derivative of the electron charge density. Furthermore, the potential is extended to short range using the universal potential of Ref. [92].

2. ACE potential

The ACE parametrization for W was trained on a large dataset of DFT data obtained using the FHI-aims all-electron code [93]. The training structures included bulk as well as defective configurations. This parametrization has been extensively tested but remains a preliminary version. The final ACE model for W will be presented in a separate publication.

3. Combined EAM and ACE potential

The AP potential for W was constructed following the strategy described in Ref. [42].

a. Optimizing the EAM potential

First, we introduce an energy offset $\Delta\xi$ since the equilibrium energies of atoms differ between the EAM and the ACE description. Thus, the embedding energy is given as

$$\xi^{\mathrm{Fit}}(\zeta) = \xi(\zeta) + \Delta\xi. \tag{B5}$$

TABLE IV. Target values with tolerance used in the loss function Eq. (B6) for the optimization of the EAM potential.

Property	Target value	Tolerance δ^{tol}
Scalar properties A_o		
Lattice parameter a_0^{bcc}	3.1840 Å	0.001 Å
Cohesive energy E_{coh}	−11.169 eV/atom	1 GPa
Bulk modulus B	279.0494 GPa	1 GPa
Elastic constant C_{11}	506.4702 GPa	1 GPa
Elastic constant C_{12}	165.3389 GPa	1 GPa
Elastic constant C_{44}	135.9924 GPa	1 GPa
Properties per structure s		
Force F	MD simulation	0.01 eV Å^{-1}
Potential energy E	MD simulation	0.01 eV

The EAM potential described by Eqs. (B2), (B3), and (B5) is optimized using atomicrex [94]. The minimized loss function is

$$\mathcal{L} = \sum_{s\in\mathcal{S}} \left\langle \left(\frac{E_{s,i}^{\text{targ}} - E_{s,i}^{\text{pred}}}{\delta_{E_{\text{md}}}^{\text{tol}}} \right)^2 + \left(\frac{\left\| \vec{F}_{s,i}^{\text{targ}} - \vec{F}_{s,i}^{\text{pred}} \right\|}{\delta_{F_{\text{md}}}^{\text{tol}}} \right)^2 \right\rangle_i + \sum_{o\in\mathcal{O}} \left(\frac{A_o^{\text{targ}} - A_o^{\text{pred}}}{\delta_o^{\text{tol}}} \right)^2, \tag{B6}$$

where the notation $\langle x_i \rangle_i = \sum_{i=1}^{N} \frac{x_i}{N}$ is used. The target values calculated with ACE and the used tolerances are given in Table IV. The optimized parameters are shown in Table V.

Just like for the EAM original potential form Ref. [55], the short-range interaction is given by the Coulomb energy screened by the ZBL screening function ϕ^{ZBL}, namely,

$$\Phi^{\text{ZBL}}(r) = \frac{1}{4\pi\epsilon_0} \frac{Z_1 Z_2 e^2}{r} \phi^{\text{ZBL}}(r), \tag{B7}$$

with the vacuum permittivity $\epsilon_0 \approx 55.26 \times 10^{-4}\, e^2/\text{eV Å}$, the nuclear charge number $Z_{1,2}$ of the respective atom. The ZBL screening function ϕ^{ZBL} is [95]

$$\phi^{\text{ZBL}} = 0.1818 e^{-3.2x^{\text{ZBL}}} + 0.5099 e^{-0.9423x^{\text{ZBL}}} + 0.2802 e^{-0.4029x^{\text{ZBL}}} + 0.02817 e^{-0.2016x^{\text{ZBL}}}, \tag{B8}$$

with the reduced distance $x^{\text{ZBL}} = r/a^{\text{ZBL}}$, where

$$a^{\text{ZBL}} = \frac{0.8854 a_0}{Z_1^{0.23} + Z_2^{0.23}}, \tag{B9}$$

where $a_0 = 0.529\,\text{Å}$ is the Bohr radius. For W-W interaction with $Z_1 = Z_2 = 74$ follows $a_{\text{ZBL}} \approx 0.0870\,\text{Å}$. The ZBL potential Φ^{ZBL} and the pair potential Φ are interpolated according to Ref. [96] between $r_{\text{lo}}^{\text{int}}$ and $r_{\text{hi}}^{\text{int}}$ with

TABLE V. Parameters of the optimized EAM potential at 300 K.

Parameter	Value	Parameter	Value
$r_{\text{lo}}^{\text{int}}$/Å	1.10002	δ_8^{Φ}/Å	3.85904
$r_{\text{hi}}^{\text{int}}$/Å	2.10004	δ_9^{Φ}/Å	4.10323
Z	74.0	δ_{10}^{Φ}/Å	4.73354
$\epsilon_0/e^2\text{eV}^{-1}\text{Å}^{-1}$	0.005526	δ_{11}^{Φ}/Å	4.8959
a_{ZBL}/Å	0.087024	δ_{12}^{Φ}/Å	5.09081
a_1^{Φ}/eV	3663.54	δ_{13}^{Φ}/Å	5.27739
a_2^{Φ}/eV	−3663.85	δ_{14}^{Φ}/Å	5.40309
a_3^{Φ}/eV	128.443	δ_{15}^{Φ}/Å	5.45078
a_4^{Φ}/eV	2.10845	a_1^{ρ}/eV	−267.394
a_5^{Φ}/eV	5.10311	a_2^{ρ}/eV	0.486763
a_6^{Φ}/eV	−4.06894	a_3^{ρ}/eV	−0.0425619
a_7^{Φ}/eV	1.25081	a_4^{ρ}/eV	0.0330214
a_8^{Φ}/eV	1.64931	δ_1^{ρ}/Å	2.5
a_9^{Φ}/eV	−1.4248	δ_2^{ρ}/Å	3.1
a_{10}^{Φ}/eV	−0.761194	δ_3^{ρ}/Å	3.5
a_{11}^{Φ}/eV	1.93524	δ_4^{ρ}/Å	4.9
a_{12}^{Φ}/eV	−0.70151	a_1^{ξ}/eV	−6.24657
a_{13}^{Φ}/eV	0.0935973	a_2^{ξ}/eV	−0.0836583
a_{14}^{Φ}/eV	−1.40395	$\Delta\xi$/eV	−2.14333
a_{15}^{Φ}/eV	1.13035	b_0^{Φ}/eV	15390.78524
δ_1^{Φ}/Å	2.74456	b_1^{Φ}/eV Å^{-1}	−41436.47926
δ_2^{Φ}/Å	2.74451	b_2^{Φ}/eV Å^{-2}	45168.43075
δ_3^{Φ}/Å	2.28653	b_3^{Φ}/eV Å^{-3}	−24693.64209
δ_4^{Φ}/Å	2.91147	b_4^{Φ}/eV Å^{-4}	6736.28696
δ_5^{Φ}/Å	2.96512	b_5^{Φ}/eV Å^{-5}	−731.61162
δ_6^{Φ}/Å	3.07694	r_{cut}^{ρ}/Å	2.46396
δ_7^{Φ}/Å	3.53116		

the polynomial

$$\Phi^{\text{int}}(x) = \sum_{m=0}^{5} b_m^{\Phi} x^m, \tag{B10}$$

so the pair potential and its first two derivatives are continuous at $r_{\text{lo}}^{\text{int}}$ and $r_{\text{hi}}^{\text{int}}$. Thereby, we get the pair potential

$$\Phi^{\text{Fit}}(r) = \begin{cases} \Phi^{\text{ZBL}}(r) & \text{for } r < r_{\text{lo}}^{\text{int}} \\ \Phi^{\text{int}}(r) & \text{for } r_{\text{lo}}^{\text{int}} \leqslant r \leqslant r_{\text{hi}}^{\text{int}} \\ \Phi(r) & \text{for } r_{\text{hi}}^{\text{int}} < r. \end{cases} \tag{B11}$$

Hence, we use the optimized EAM potential described by Eqs. (B4), (B5), and (B11) with the parameters given in Table V. Basic properties calculated with the optimized EAM potential compared with the original EAM potential and the ACE potential are shown in Table VI. The elastic constants and related bulk properties correspond to the ACE reference values. Properties not included in the atomicrex optimization, such as surface energies or formation energies of interstitials,

TABLE VI. Properties calculated with tungsten potentials.

		EAM	
	ACE	Fit	Original
Interstitial formation energy/eV			
100 dumbbell/eV	12.47	8.77	12.94
Tetrahedral/eV	11.03	8.66	10.43
Elastic constant C_{11}/GPa	506	508	523
Elastic constant C_{12}/GPa	165	162	203
Elastic constant C_{44}/GPa	136	140	160
Bulk modulus/GPa	279	277	310
Shear modulus 1/GPa	136	140	160
Shear modulus 2/GPa	171	173	160
Poisson ratio	0.25	0.24	0.28
Lattice constant/A	3.1840	3.1837	3.1400
Cohesive energy/eV	−11.17	−11.17	−8.90
Vacancy formation energy (bcc)/eV	3.36	4.01	3.49
Surface energy 111/Jm^{-2}	3.62	3.55	2.96
Surface energy 100/Jm^{-2}	4.11	3.10	2.72
Surface energy 110/Jm^{-2}	3.51	2.95	2.31

are not reproduced. The phonon spectra of the optimized EAM potential and the ACE potential compared in Fig. 14 are in good agreement.

b. Switching function

The parameters of the switching function λ are set according to the strategy used in Ref. [42]. The used values are shown in Table VII. The centrosymmetry parameter uses neighboring atoms which are on opposite positions of the central atom and is usually calculated for the atoms of the nearest-neighbor shell [49]. The distance in a bcc lattice between the first- and second-neighbor shell is with $(1-\sqrt{3}/2) \approx 0.13$ lattice constants relatively small, whereas

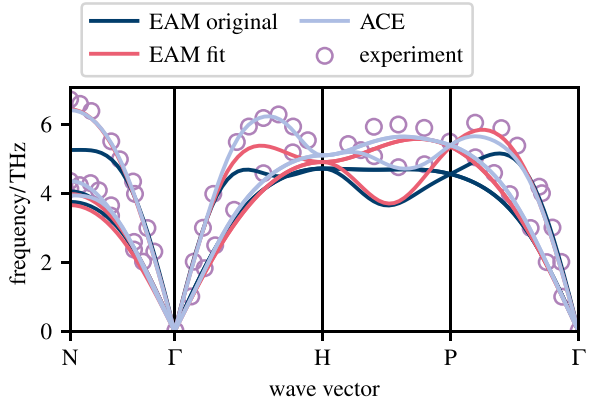

FIG. 14. Phonon spectra calculated with ASE [97] of the fitted EAM potential, original EAM potential, the ACE potential, and experimental values [98] measured by inelastic neutron scattering at room temperature.

TABLE VII. Parameters of the adaptive-precision model and values of the parameters for tungsten at 300 K.

Parameter	Value	Parameter	Value	Parameter	Value
N_{buffer}	0 atoms	CSP_{hi}	1.6 Å^2	$N_{\lambda,\text{avg}}$	110
$N_{\text{CSP,avg}}$	110	$r_{\lambda,\text{lo}}$	4.0 Å	$\Delta\lambda_{\text{min}}$	0.01
CSP_{lo}	1.5 Å^2	$r_{\lambda,\text{hi}}$	12.0 Å	$\lvert\Omega_i\rvert$	800 atoms

the distance between the second- and third-neighbor shell is $(\sqrt{2}-1) \approx 0.41$ lattice constants. Therefore, one can easily separate the third from the first two neighbor shells. Thus, we calculate the CSP with 14 nearest-neighboring atoms which corresponds to the number of neighbors in the first two neighbor shells.

APPENDIX C: COMPUTATIONAL EFFICIENCY

The computational time required for the simulation of the nanoindentations are reported in Figs. 2 and 8 for the whole nanoindentation. The automatic precision adjustment during the AP simulations also affects the computational time, which is why an analysis of the computational time dependent on the progress of the simulation provides further insights. LAMMPS measures the number of simulated time steps per wall-time second. The computational time τ_{atom} per atom and time step is given as

$$\tau_{\text{atom}} = \frac{\text{No. processors}}{\text{No. time steps per wall-time second} \times \text{No. particles}}, \tag{C1}$$

which is shown in Fig. 15(a) dependent on the simulated time. τ_{atom} is approximately constant for EAM and ACE for the whole simulation, while τ_{atom} starts to increase during the AP simulations. The number of precisely calculated atoms increases during the simulation, as the dislocation density ρ^{dxa} [Eq. (10)] increases (cf. Figs. 6 and 13). As the number of precisely calculated atoms and τ_{atom} are positively correlated [cf. Fig. 15(c)], the increase of τ_{atom} over time is expected.

The imbalance I is defined in LAMMPS as [99]

$$I = \frac{\max\left\{\tau_p^{\text{force}}\right\}}{\left\langle\tau_p^{\text{force}}\right\rangle_p}, \tag{C2}$$

where τ_p^{force} denotes the on processor p measured force-calculation time. $I = 1$ applies for a perfectly balanced system, while $I > 1$ indicates load imbalances. The mean imbalance in the adaptive-precision simulations of W and Cu is 1.09 and 1.29, whereas the visualization dependent on the simulated time in Fig. 15(b) shows for Cu a decrease of the imbalance when τ_{atom} increases. Hence, the increase of τ_{atom} in the AP simulations is independent of the imbalance for W and weakened by the imbalance for Cu. Furthermore, the fixing of the switching parameter in the zones of interest, as described in Sec. II B 3, results in a decrease of the imbalance of 0.12 in the AP Cu simulation compared to the AP Cu simulation in Ref. [42]. Thermal fluctuations of atoms affect the centrosymmetry parameter, which is used to calculate the switching parameter. As discussed in Ref. [42], an atom, which is only due to thermal fluctuations detected for a precise calculation,

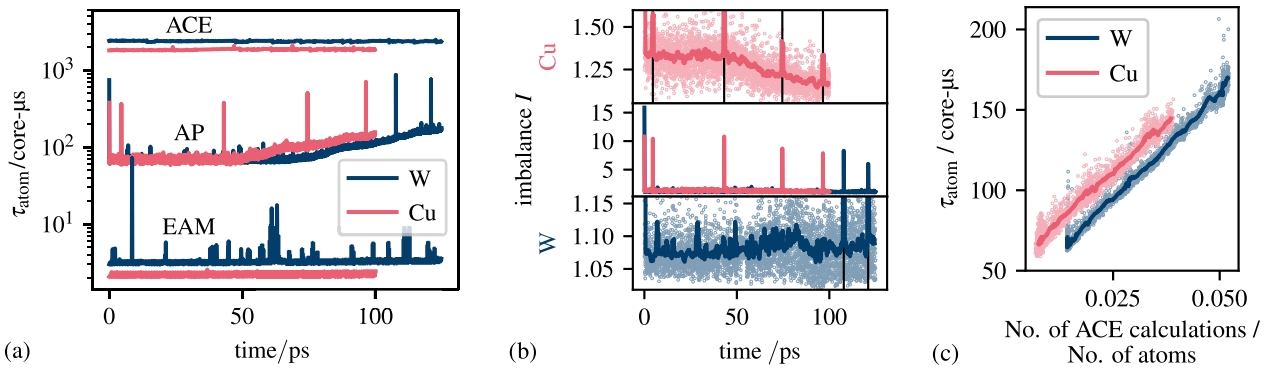

FIG. 15. (a) Computing time τ_{atom} per atom and time step according to Eq. (C1), dependent on the simulated time for all nanoindentations. (b) Imbalance I according to Eq. (C2), dependent on the simulated time for the AP simulations. The central plot shows that the system is unbalanced at the beginning and at restarts of the simulation. The part of the imbalance axis corresponding to a balanced system, i.e., $I \approx 1$, is enlarged at the top for Cu and at the bottom for W. The time of restart is marked with vertical lines in the enlarged plots. (c) Correlation of τ_{atom} and the number of precisely calculated atoms. All measured values in (c) and in the enlarged plots in (b) are shown as points, while a moving average of 1 ps intervals is shown as a line.

causes due to the spatial transition zone the computation of ACE also for neighboring atoms and, thereby, increases the imbalance. The existence of such atoms at room temperature is less likely for W than for Cu due to the higher melting point of W. Therefore, the imbalance I is smaller for W than for Cu in the AP nanoindentations [cf. Fig. 15(b)]. As the number of fast calculated atoms decreases over time, in particular, through the gliding of prismatic dislocation loops (cf. Fig. 5), the number of atoms, that are susceptible to incorrect precise treatment and, thus, the imbalance decrease at the end of the AP Cu simulation.

APPENDIX D: TUNGSTEN NANOINDENTATION WITH OPTIMIZED EAM POTENTIAL

To validate whether the nanoindentation simulation of W with the optimized EAM potential would give results similar to the reference ACE potential, we performed an additional simulation run. Dislocation lines, defects, and the shear strain from this simulation are visualized in Fig. 16 for the same indentation depths as in Figs. 11 and 12.

For the normalized indentation depth $h/a_c \approx 0.41$ (left column), there are primarily nonscrew dislocations detected by the BDA algorithm for the original EAM potential [cf. Fig. 11(g)] as well as for the optimized EAM potential [cf. Fig. 16(e)]. Unlike in the AP/ACE simulations, no twins are detected.

At the maximum indentation depth (right column), we observe less pileup when the optimized EAM potential is used than when the original EAM potential is used [cf. Figs. 16(d) and 12(a)]. Furthermore, twins are detected by BDA in the optimized-EAM nanoindentation [cf. Fig. 16(d)] while there are none in the original-EAM nanoindentation. However, there are still numerous ⟨100⟩ dislocation lines below the indenter [cf. Fig. 16(b)] and the shear strain is higher only below the indenter for both EAM potentials [cf. Figs. 16(h) and 12(j)], in contrast to the $1/2\langle 111\rangle$ loops observed in the AP/ACE nanoindentation.

In conclusion, the optimized EAM potential predicts a less pronounced pileup at the indent's rim and the existence of twins, unlike the original EAM potential, which somewhat resemble the AP/ACE results. However, the dislocation mechanisms remain the same as for the original EAM potential. Therefore, the mechanisms observed in the AP/ACE nanoindentation simulations cannot be simply achieved via optimization of the EAM potential.

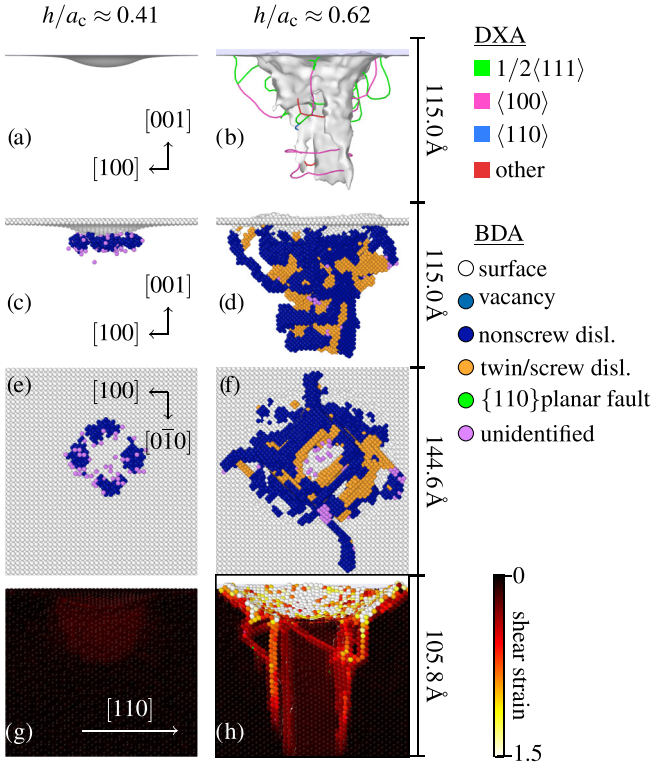

FIG. 16. Tungsten nanoindentation simulated with the optimized EAM potential (Table V) visualized with (a), (b) the dislocation extraction algorithm (DXA) and (c)–(f) the bcc defect analysis (BDA). (g), (h) A cut in the $(1\bar{1}0)$ plane through the contact point is used to visualize the by OVITO calculated shear strain. Scale bars are given on the right side of each row.

[1] U. Landman, W. D. Luedtke, N. A. Burnham, and R. J. Colton, Atomistic mechanisms and dynamics of adhesion, nanoindentation, and fracture, Science **248**, 454 (1990).

[2] W. G. Hoover, A. J. De Groot, C. G. Hoover, I. F. Stowers, T. Kawai, B. L. Holian, T. Boku, S. Ihara, and J. Belak, Large-scale elastic-plastic indentation simulations via nonequilibrium molecular dynamics, Phys. Rev. A **42**, 5844 (1990).

[3] M. S. Daw, S. M. Foiles, and M. I. Baskes, The embedded-atom method: A review of theory and applications, Mater. Sci. Rep. **9**, 251 (1993).

[4] M. W. Finnis and J. E. Sinclair, A simple empirical n-body potential for transition metals, Philos. Mag. A **50**, 45 (1984).

[5] D. G. Pettifor, *Bonding and Structure of Molecules and Solids* (Oxford University Press, Oxford, 1995).

[6] M. Mrovec, D. Nguyen-Manh, D. G. Pettifor, and V. Vitek, Bond-order potential for molybdenum: Application to dislocation behavior, Phys. Rev. B **69**, 094115 (2004).

[7] M. Mrovec, R. Gröger, A. G. Bailey, D. Nguyen-Manh, C. Elsässer, and V. Vitek, Bond-order potential for simulations of extended defects in tungsten, Phys. Rev. B **75**, 104119 (2007).

[8] R. Gröger, A. G. Bailey, and V. Vitek, Multiscale modeling of plastic deformation of molybdenum and tungsten: I. Atomistic studies of the core structure and glide of 1/2⟨111⟩ screw dislocations at 0 K, Acta Mater. **56**, 5401 (2008).

[9] A. G. Marinopoulos, V. Vitek, and A. E. Carlsson, Significance of non-central forces in atomistic studies of grain boundaries in bcc transition metals, Philos. Mag. A **72**, 1311 (1995).

[10] C. C. Matthai, P. J. Grout, and N. H. March, Interatomic forces in the b.c.c. transition metals, J. Phys. Chem. Solids **42**, 317 (1981).

[11] R. Gröger and V. Vitek, Directional versus central-force bonding in studies of the structure and glide of 1/2⟨111⟩ screw dislocations in bcc transition metals, Philos. Mag. **89**, 3163 (2009).

[12] J. J. Möller, M. Mrovec, I. Bleskov, J. Neugebauer, T. Hammerschmidt, R. Drautz, C. Elsässer, T. Hickel, and E. Bitzek, {110} planar faults in strained bcc metals: Origins and implications of a commonly observed artifact of classical potentials, Phys. Rev. Mater. **2**, 093606 (2018).

[13] M. Rieth, S. L. Dudarev, S. M. Gonzalez de Vicente, J. Aktaa, T. Ahlgren, S. Antusch, D. E. J. Armstrong, M. Balden, N. Baluc, M.-F. Barthe *et al.*, Recent progress in research on tungsten materials for nuclear fusion applications in europe, J. Nucl. Mater. **432**, 482 (2013).

[14] R. A. Pitts, S. Carpentier, F. Escourbiac, T. Hirai, V. Komarov, A. S. Kukushkin, S. Lisgo, A. Loarte, M. Merola, R. Mitteau *et al.*, Physics basis and design of the ITER plasma-facing components, J. Nucl. Mater. **415**, S957 (2011).

[15] P. Jenuš, A. Abram, S. Novak, M. Kelemen, M. Peovnik, T. Schwarz-Selinger, and S. Markelj, Deuterium retention in tungsten, tungsten carbide and tungsten-ditungsten carbide composites, J. Nucl. Mater. **581**, 154455 (2023).

[16] P. Hansson, Influence of the crystallographic orientation and thickness of thin copper coatings during nanoindentation, Eng. Fract. Mech. **150**, 143 (2015).

[17] I. H. Sahputra, Temperature and indenter radius effects on mechanical properties of copper during nanoindentation: A molecular dynamic simulation study, Eur. Phys. J. B **94**, 237 (2021).

[18] A. B. Shinde, A. Owhal, A. Sharma, P. Ranjan, T. Roy, and R. Balasubramaniam, Comparative analysis of mechanical properties for mono and poly-crystalline copper under nanoindentation insights from molecular dynamics simulations, Mater. Chem. Phys. **277**, 125559 (2022).

[19] J. Huang, Y. Liu, X. Yu, Y. Huang, G. Liu, Z. Huang, and D. Fan, Nano mechanical property analysis of single crystal copper using Berkovich nano indenter and molecular dynamic simulation, Comput. Mater. Sci. **188**, 110237 (2021).

[20] S. Goel, G. Cross, A. Stukowski, E. Gamsjäger, B. Beake, and A. Agrawal, Designing nanoindentation simulation studies by appropriate indenter choices: Case study on single crystal tungsten, Comput. Mater. Sci. **152**, 196 (2018).

[21] F. J. Domínguez-Gutiérrez, P. Grigorev, A. Naghdi, J. Byggmästar, G. Y. Wei, T. D. Swinburne, S. Papanikolaou, and M. J. Alava, Nanoindentation of tungsten: From interatomic potentials to dislocation plasticity mechanisms, Phys. Rev. Mater. **7**, 043603 (2023).

[22] Y. Hu, J. Xu, L. Su, X. Liu, Y. Zhang, S. Ding, R. Wang, and R. X. and, Nanoindentation characteristics of nanocrystalline tungsten via atomistic simulation, Philos. Mag. **103**, 749 (2023).

[23] F. Zhu, J. Tao, J. Wu, F. Zhou, J. Chen, Y. Pei, L. Song, J. Wu, and D. Wang, Molecular dynamics simulation of the indentation behavior of tungsten with varying crystal orientations and Berkovich indenter orientations, Mater. Today Commun. **41**, 110738 (2024).

[24] D. Xu, Z. Huang, L. Xu, G. Yin, Y. Lin, Q. Shen, and F. Chen, Enhancing surface strength of tungsten by gradient nanograined structure, J. Appl. Phys. **135**, 195101 (2024).

[25] T. Karafi, A. Tahiri, H. Chabba, M. Idiri, and B. Boubeker, Effect of grain-size in nanocrystalline tungsten on hardness and dislocation density: A molecular dynamics study, Crystals **13**, 469 (2023).

[26] J. S. Smith, B. Nebgen, N. Mathew, J. Chen, N. Lubbers, L. Burakovsky, S. Tretiak, H. A. Nam, T. Germann, S. Fensin *et al.*, Automated discovery of a robust interatomic potential for aluminum, Nat. Commun. **12**, 1257 (2021).

[27] Y. Lysogorskiy, C. van der Oord, A. Bochkarev, S. Menon, M. Rinaldi, T. Hammerschmidt, M. Mrovec, A. Thompson, G. Csányi, C. Ortner *et al.*, Performant implementation of the atomic cluster expansion (PACE) and application to copper and silicon, npj Comput. Mater. **7**, 97 (2021).

[28] M. Hodapp, Machine learning is funny but physics makes the money: How machine-learning potentials can advance computer-aided materials design in metallurgy, Comput. Mater. Sci. **233**, 112715 (2024).

[29] Y. Mishin, Machine-learning interatomic potentials for materials science, Acta Mater. **214**, 116980 (2021).

[30] B. Mortazavi, Recent advances in machine learning-assisted multiscale design of energy materials, Adv. Energy Mater. **15**, 2403876 (2025).

[31] M. A. Wood, M. A. Cusentino, B. D. Wirth, and A. P. Thompson, Data-driven material models for atomistic simulation, Phys. Rev. B **99**, 184305 (2019).

[32] G. Nikoulis, J. Byggmästar, J. Kioseoglou, K. Nordlund, and F. Djurabekova, Machine-learning interatomic potential for W-Mo alloys, J. Phys.: Condens. Matter **33**, 315403 (2021).

[33] J. Byggmästar, K. Nordlund, and F. Djurabekova, Simple machine-learned interatomic potentials for complex alloys, Phys. Rev. Mater. **6**, 083801 (2022).

[34] E. Cho, W.-J. Son, E. Cho, I. Jang, D. S. Kim, and K. Min, Atomistic insights into adhesion characteristics of tungsten on titanium nitride using steered molecular dynamics with machine learning interatomic potential, Sci. Rep. **13**, 17145 (2023).

[35] J. Liu, J. Byggmästar, Z. Fan, P. Qian, and Y. Su, Large-scale machine-learning molecular dynamics simulation of primary radiation damage in tungsten, Phys. Rev. B **108**, 054312 (2023).

[36] M. Qamar, M. Mrovec, Y. Lysogorskiy, A. Bochkarev, and R. Drautz, Atomic cluster expansion for quantum-accurate large-scale simulations of carbon, J. Chem. Theory Comput. **19**, 5151 (2023).

[37] W. G. Stark, C. van der Oord, I. Batatia, Y. Zhang, B. Jiang, G. Csányi, and R. J. Maurer, Benchmarking of machine learning interatomic potentials for reactive hydrogen dynamics at metal surfaces, Mach. Learn.: Sci. Technol. **5**, 030501 (2024).

[38] A. Warshel and M. Levitt, Theoretical studies of enzymic reactions: Dielectric, electrostatic and steric stabilization of the carbonium ion in the reaction of lysozyme, J. Mol. Biol. **103**, 227 (1976).

[39] M. J. Buehler, A. C. T. van Duin, and W. A. Goddard, Multiparadigm modeling of dynamical crack propagation in silicon using a reactive force field, Phys. Rev. Lett. **96**, 095505 (2006).

[40] T. Kerdcharoen, K. R. Liedl, and B. M. Rode, A QM/MM simulation method applied to the solution of li+ in liquid ammonia, Chem. Phys. **211**, 313 (1996).

[41] A. Heyden, H. Lin, and D. G. Truhlar, Adaptive partitioning in combined quantum mechanical and molecular mechanical calculations of potential energy functions for multiscale simulations, J. Phys. Chem. B **111**, 2231 (2007).

[42] D. Immel, R. Drautz, and G. Sutmann, Adaptive-precision potentials for large-scale atomistic simulations, J. Chem. Phys. **162**, 114119 (2025).

[43] F. Birks, T. D. Swinburne, and J. R. Kermode, Efficient and accurate spatial mixing of machine learned interatomic potentials for materials science, arXiv:2502.19081.

[44] L. Zhang, H. Wang, and W. E, Adaptive coupling of a deep neural network potential to a classical force field, J. Chem. Phys. **149**, 154107 (2018).

[45] L. Böselt, M. Thürlemann, and S. Riniker, Machine learning in QM/MM molecular dynamics simulations of condensed-phase systems, J. Chem. Theory Comput. **17**, 2641 (2021).

[46] T. P. Remington, C. J. Ruestes, E. M. Bringa, B. A. Remington, C. H. Lu, B. Kad, and M. A. Meyers, Plastic deformation in nanoindentation of tantalum: A new mechanism for prismatic loop formation, Acta Mater. **78**, 378 (2014).

[47] A. P. Thompson, H. M. Aktulga, R. Berger, D. S. Bolintineanu, W. M. Brown, P. S. Crozier, P. J. in 't Veld, A. Kohlmeyer, S. G. Moore, T. D. Nguyen *et al.*, LAMMPS: A flexible simulation tool for particle-based materials modeling at the atomic, meso, and continuum scales, Comput. Phys. Commun. **271**, 108171 (2022).

[48] H.-T. Luu, S.-L. Dang, T.-V. Hoang, and N. Gunkelmann, Molecular dynamics simulation of nanoindentation in Al and Fe: On the influence of system characteristics, Appl. Surf. Sci. **551**, 149221 (2021).

[49] C. L. Kelchner, S. J. Plimpton, and J. C. Hamilton, Dislocation nucleation and defect structure during surface indentation, Phys. Rev. B **58**, 11085 (1998).

[50] Y. Mishin, M. J. Mehl, D. A. Papaconstantopoulos, A. F. Voter, and J. D. Kress, Structural stability and lattice defects in copper: *Ab initio*, tight-binding, and embedded-atom calculations, Phys. Rev. B **63**, 224106 (2001).

[51] A. Hernandez, A. Balasubramanian, F. Yuan, S. A. M. Mason, and T. Mueller, Fast, accurate, and transferable many-body interatomic potentials by symbolic regression, npj Comput. Mater. **5**, 112 (2019).

[52] H. S. Huang, L. Q. Ai, A. C. T. van Duin, M. Chen, and Y. J. Lü, ReaxFF reactive force field for molecular dynamics simulations of liquid Cu and Zr metals, J. Chem. Phys. **151**, 094503 (2019).

[53] D. Geissler, J. Freudenberger, A. Kauffmann, S. Martin, and D. Rafaja, Assessment of the thermodynamic dimension of the stacking fault energy, Philos. Mag. **94**, 2967 (2014).

[54] E. M. Bringa, J. U. Cazamias, P. Erhart, J. Stölken, N. Tanushev, B. D. Wirth, R. E. Rudd, and M. J. Caturla, Atomistic shock Hugoniot simulation of single-crystal copper, J. Appl. Phys. **96**, 3793 (2004).

[55] M.-C. Marinica, L. Ventelon, M. R. Gilbert, L. Proville, S. L. Dudarev, J. Marian, G. Bencteux, and F. Willaime, Interatomic potentials for modelling radiation defects and dislocations in tungsten, J. Phys.: Condens. Matter **25**, 395502 (2013).

[56] G. Bonny, P. Grigorev, and D. Terentyev, On the binding of nanometric hydrogen-helium clusters in tungsten, J. Phys.: Condens. Matter **26**, 485001 (2014).

[57] W. H. Zhou, C. G. Zhang, Y. G. Li, and Z. Zeng, Transport, dissociation and rotation of small self-interstitial atom clusters in tungsten, J. Nucl. Mater. **453**, 202 (2014).

[58] M. E. Stupak, M. G. Urazaliev, and V. V. Popov, Structure and energy of ⟨110⟩ symmetric tilt boundaries in polycrystalline tungsten, Phys. Met. Metallogr. **121**, 797 (2020).

[59] N. C. Nguyen and A. Rohskopf, Proper orthogonal descriptors for efficient and accurate interatomic potentials, J. Comput. Phys. **480**, 112030 (2023).

[60] S. Menon, Y. Lysogorskiy, J. Rogal, and R. Drautz, Automated free-energy calculation from atomistic simulations, Phys. Rev. Mater. **5**, 103801 (2021).

[61] R. Dsouza, M. Poul, L. Huber, T. D. Swinburne, and J. Neugebauer, Sampling-free computation of finite temperature material properties in isochoric and isobaric ensembles using the mean-field anharmonic bond model, Phys. Rev. B **109**, 064108 (2024).

[62] R. Namakian, D. Moldovan, and T. D. Swinburne, Temperature dependent stacking fault free energy profiles and partial dislocation separation in fcc Cu, Comput. Mater. Sci. **218**, 111971 (2023).

[63] P. Thörnig, JURECA: Data centric and booster modules implementing the modular supercomputing architecture at Jülich supercomputing centre, J. Large-Scale Res. Facilities (JLSRF) **7**, A182 (2021) [Translation: On the contact of elastic solids].

[64] H. Hertz, Ueber die Berührung fester elastischer Körper, J. Angew. Math. **1882**, 156 (1882).

[65] C. J. Ruestes, A. Stukowski, Y. Tang, D. R. Tramontina, P. Erhart, B. A. Remington, H. M. Urbassek, M. A. Meyers, and E. M. Bringa, Atomistic simulation of tantalum nanoindentation: Effects of indenter diameter, penetration velocity, and interatomic potentials on defect mechanisms and evolution, Mater. Sci. Eng.: A **613**, 390 (2014).

[66] G. Ziegenhain, H. M. Urbassek, and A. Hartmaier, Influence of crystal anisotropy on elastic deformation and onset of plasticity in nanoindentation: A simulational study, J. Appl. Phys. **107**, 061807 (2010).

[67] J. J. Vlassak and W. D. Nix, Indentation modulus of elastically anisotropic half spaces, Philos. Mag. A **67**, 1045 (1993).
[68] J. J. Vlassak and W. D. Nix, Measuring the elastic properties of anisotropic materials by means of indentation experiments, J. Mech. Phys. Solids **42**, 1223 (1994).
[69] J. Varillas Delgado, A molecular dynamics study of nanocontact plasticity and dislocation avalanches in FCC and BCC crystals, Ph.D. thesis, Universitat Politècnica de Catalunya, Departament de Ciència dels Materials i Enginyeria Metallúrgica, 2019.
[70] I. Muhammad, H. Fayyaz, R. Muhammad, and A. S. A., Dynamic characteristics of nanoindentation in Ni: A molecular dynamics simulation study, Chin. Phys. B **21**, 116201 (2012).
[71] T.-H. Fang, S.-R. Jian, and D.-S. Chuu, Molecular dynamics analysis of effects of velocity and loading on the nanoindentation, Jpn. J. Appl. Phys. **41**, L1328 (2002).
[72] A. Stukowski, V. V. Bulatov, and A. Arsenlis, Automated identification and indexing of dislocations in crystal interfaces, Modell. Simul. Mater. Sci. Eng. **20**, 085007 (2012).
[73] A. Stukowski, Visualization and analysis of atomistic simulation data with ovitothe open visualization tool, Modell. Simul. Mater. Sci. Eng. **18**, 015012 (2010).
[74] K. Durst, B. Backes, and M. Göken, Indentation size effect in metallic materials: Correcting for the size of the plastic zone, Scr. Mater. **52**, 1093 (2005).
[75] Z. Wang, J. Zhang, A. Ma, A. Hartmaier, Y. Yan, and T. Sun, On the crystallographic anisotropy of plastic zone size in single crystalline copper under Berkovich nanoindentation, Mater. Today Commun. **25**, 101314 (2020).
[76] C. Begau, J. Hua, and A. Hartmaier, A novel approach to study dislocation density tensors and lattice rotation patterns in atomistic simulations, J. Mech. Phys. Solids **60**, 711 (2012).
[77] F. Shimizu, S. Ogata, and J. Li, Theory of shear banding in metallic glasses and molecular dynamics calculations, Mater. Trans. **48**, 2923 (2007).
[78] F. J. Dominguez-Gutierrez, P. Grigorev, A. Naghdi, Q. Q. Xu, J. Byggmastar, G. Y. Wei, T. D. Swinburne, S. Papanikolaou, and M. J. Alava, Atomistic simulations of nanoindentation in single crystalline tungsten: The role of interatomic potentials, arXiv:2205.09165.
[79] A. P. Bartók, M. C. Payne, R. Kondor, and G. Csányi, Gaussian approximation potentials: The accuracy of quantum mechanics, without the electrons, Phys. Rev. Lett. **104**, 136403 (2010).
[80] X. W. Zhou, R. A. Johnson, and H. N. G. Wadley, Misfit-energy-increasing dislocations in vapor-deposited CoFe/NiFe multilayers, Phys. Rev. B **69**, 144113 (2004).
[81] J. J. Möller and E. Bitzek, BDA: A novel method for identifying defects in body-centered cubic crystals, MethodsX **3**, 279 (2016).
[82] A. D. Naghdi, F. Pellegrini, E. Kkbenli, D. Massa, F. J. Dominguez-Gutierrez, E. Kaxiras, and S. Papanikolaou, Neural network interatomic potentials for open surface nanomechanics applications, Acta Mater. **277**, 120200 (2024).
[83] J. D. Honeycutt and H. C. Andersen, Molecular dynamics study of melting and freezing of small Lennard-Jones clusters, J. Phys. Chem. **91**, 4950 (1987).
[84] J. Wang, Z. Zeng, C. R. Weinberger, Z. Zhang, T. Zhu, and S. X. Mao, *In situ* atomic-scale observation of twinning-dominated deformation in nanoscale body-centred cubic tungsten, Nat. Mater. **14**, 594 (2015).
[85] J. Alcalá, R. Dalmau, O. Franke, M. Biener, J. Biener, and A. Hodge, Planar defect nucleation and annihilation mechanisms in nanocontact plasticity of metal surfaces, Phys. Rev. Lett. **109**, 075502 (2012).
[86] S. Plimpton, Fast parallel algorithms for short-range molecular dynamics, J. Comput. Phys. **117**, 1 (1995).
[87] https://github.com/lammps/lammps.
[88] P. G. Heighway, D. McGonegle, N. Park, A. Higginbotham, and J. S. Wark, Molecular dynamics simulations of grain interactions in shock-compressed highly textured columnar nanocrystals, Phys. Rev. Mater. **3**, 083602 (2019).
[89] R. Halver, Adaptives Lastbalance-Verfahren für Gebietszerlegung in der Molekulardynamik, Master's thesis, FH Aachen University of Applied Sciences, 2010.
[90] R. Halver, S. Schulz, and G. Sutmann, ALL: A loadbalancing library, C++/Fortran library, https://gitlab.version.fz-juelich.de/SLMS/loadbalancing/-/releases.
[91] Berger and Bokhari, A partitioning strategy for nonuniform problems on multiprocessors, IEEE Trans. Comput. **C-36**, 570 (1987).
[92] J. F. Ziegler and J. P. Biersack, The stopping and range of ions in matter, in *Treatise on Heavy-Ion Science*, edited by D. Allan Bromley, Astrophysics, Chemistry, and Condensed Matter Vol. 6 (Springer US, Boston, MA, 1985), pp. 93–129.
[93] V. Blum, R. Gehrke, F. Hanke, P. Havu, V. Havu, X. Ren, K. Reuter, and M. Scheffler, *Ab initio* molecular simulations with numeric atom-centered orbitals, Comput. Phys. Commun. **180**, 2175 (2009).
[94] A. Stukowski, E. Fransson, M. Mock, and P. Erhart, Atomicrexa general purpose tool for the construction of atomic interaction models, Modell. Simul. Mater. Sci. Eng. **25**, 055003 (2017).
[95] J. P. Biersack and J. F. Ziegler, The stopping and range of ions in solids, in *Ion Implantation Techniques*, edited by Heiner Ryssel and Hans Glawischnig (Springer, Berlin, 1982), pp. 122–156.
[96] C. Björkas, K. Nordlund, and S. Dudarev, Modelling radiation effects using the *ab initio* based tungsten and vanadium potentials, Nucl. Instrum. Methods Phys. Res. B **267**, 3204 (2009).
[97] A. H. Larsen, J. J. Mortensen, J. Blomqvist, I. E. Castelli, R. Christensen, M. Duak, J. Friis, M. N. Groves, B. Hammer, C. Hargus *et al.*, The atomic simulation environment—A Python library for working with atoms, J. Phys.: Condens. Matter **29**, 273002 (2017).
[98] S. H. Chen and B. N. Brockhouse, Lattice vibrations of tungsten, Solid State Commun. **2**, 73 (1964).
[99] LAMMPS, LAMMPS documentation: fix balance command, https://docs.lammps.org/fix_balance.html.